Published in final edited form as:

Clin Cancer Res. 2016 June 15; 22(12): 2950–2959. doi:10.1158/1078-0432.CCR-15-2115.

Alternate metabolic programs define regional variation of relevant biological features in renal cell carcinoma progression

Samira A. Brooks[1,2], **Amir H. Khandani**[*,3,5], **Julia R. Fielding**[3], **Weili Lin**[3], **Tiffany Sills**[4], **Yueh Lee**[3], **Alexandra Arreola**[1], **Mathew I. Milowsky**[1,4], **Eric M. Wallen**[1,4], **Michael E. Woods**[3], **Angie B. Smith**[4], **Mathew E. Nielsen**[4], **Joel S. Parker**[1,7], **David S. Lalush**[5], and **W. Kimryn Rathmell**[*,1,4,7]

[1] UNC Lineberger Comprehensive Cancer Center, Chapel Hill, NC, USA

[2] Curriculum in Toxicology, University of North Carolina at Chapel Hill, Chapel Hill, NC, USA

[3] Department of Radiology, University of North Carolina, Chapel Hill, NC, USA

[4] Department of Urology, University of North Carolina at Chapel Hill, Chapel Hill, NC, USA

[5] Department of Radiology, Nuclear Medicine, University of North Carolina at Chapel Hill, NC, USA

[6] Joint Department of Biomedical Engineering, The University of North Carolina at Chapel Hill and North Carolina State University, Chapel Hill, Raleigh, NC, USA

[7] Department of Genetics, University of North Carolina at Chapel Hill, Chapel Hill, NC, USA

Abstract

Purpose—ccRCC has recently been redefined as a highly heterogeneous disease. In addition to genetic heterogeneity, the tumor displays risk variability for developing metastatic disease, therefore underscoring the urgent need for tissue-based prognostic strategies applicable to the clinical setting. We've recently employed the novel positron emission tomography/magnetic resonance (PET/MR) image modality to enrich our understanding of how tumor heterogeneity can relate to gene expression and tumor biology to assist in defining individualized treatment plans.

Experimental Design—ccRCC patients underwent PET/MR imaging, and these images subsequently used to identify areas of varied intensity for sampling. Samples from eight patients were subjected to histological, immunohistochemical, and microarray analysis.

Results—Tumor subsamples displayed a range of heterogeneity for common features of HIF expression and microvessel density, as well as for features closely linked to metabolic processes, such as GLUT1 and FBP1. In addition, gene signatures linked with disease risk (ccA and ccB) also demonstrated variable heterogeneity, with most tumors displaying a dominant panel of features across the sampled regions. Intriguingly, the ccA and ccB-classified samples

[*]Correspondence to: W. Kimryn Rathmell, MD, PhD, 450 West Drive, CB 7295, University of North Carolina, Chapel Hill, NC 27599, TEL: 919-966-8644, FAX: 919-966-8212, Rathmell@med.unc.edu.

W. Kimryn Rathmell certifies that all conflicts of interest, including specific financial interests and relationships and affiliations relevant to the subject matter or materials discussed in the manuscript are the following: J.S. Parker has consulted for NanoString Technologies, and W.K. Rathmell has a patent filed on the ClearCode test.

corresponded with metabolic features and functional imaging levels. These correlations further linked a variety of metabolic pathways (i.e. the pentose phosphate and mTOR pathways) with the more aggressive, and glucose avid ccB subtype.

Conclusions—Higher tumor dependency on exogenous glucose accompanies the development of features associated with the poor risk ccB subgroup. Linking these panels of features may provide the opportunity to create functional maps to enable enhanced visualization of the heterogeneous biological processes of an individual's disease.

Keywords

Glucose; PET; FBP-1; renal cell carcinoma; kidney cancer

Introduction

The heterogeneous biology of most cancers challenges tools that rely on single biopsy criteria for making disease-wide assessments. Sporadic clear cell renal cell carcinoma (ccRCC) has recently been recognized to display a high level of genetic heterogeneity, based on high-throughput sequencing studies of subsampled tumors. These findings reveal a core mutational signature, which likely represents early or initiating events, coupled with variable secondary mutations, some of which are presumed to be associated with disease progression(1, 2). Other recent studies have suggested that single biopsies are inadequate to fully evaluate the molecular and genetic features of ccRCC, implying the need for multiple sampling in biomarker development, or novel alternatives to assess the disease more globally in an individual patient(3).

In addition, recent studies have implicated changes in hypoxia-regulated gene expression, and key enzymes involved in cellular metabolic programs, as potential features linked with progression(4, 5). In particular, the recent finding of lost fructose 1,6 bisphosphatase 1 (FBP1) expression in renal tumors implies that metabolic diversions are central to ccRCC disease progression (6). The regional variation of these and other relevant protein features of ccRCC, or the associations with regional metabolic variation has not been explored previously. Here, we use positron emission tomography (PET) with fluoridated 2-deoxyglucose (FDG) in combination with magnetic resonance imaging for structural and anatomic resolution, gene expression, and protein marker analysis. This approach permits evaluation of the potential for metabolic imaging to provide an assessment of disease biology on regional variation in key physiological mechanisms driving tumorigenesis and tumor heterogeneity.

Materials and Methods

Patients and clinical samples

All patients were enrolled to an investigator-initiated trial, LCCC1213, using a UNC Biomedical IRB approved consent. Enrollment criteria consisted of adequate organ function, radiographic confirmation of a renal mass of sufficient size to allow subsampling, and a scheduled surgery date. Patients were encouraged to be fasting at the time of the scan, and blood sugar was tested prior to imaging. No patients were excluded due to hyperglycemia. In

total, 13 patients were imaged, but only clear cell RCC patients were included in the primary analysis (Supplemental Table S1 and 2), due to the markedly differing biology of other subtypes such as papillary RCC(5, 7, 8).

Specimens were collected from October 2012 through September 2013 at the University of North Carolina directly from the pathology grossing area using the PET/MR image map as a guide to select samples corresponding to the desired region of interest. At least five fresh kidney specimens were obtained from each patient and were transported back to the lab, relabeled, and stored as flash frozen or paraffin embedded specimens for batched analysis. However, only samples with high RNA quality were used for analysis. Stage was classified using the American Joint Committee on Cancer's Cancer Staging Manuel, 7th edition (AJCC-7). A genitourinary oncologist verified pathologic clinical variables.

PET/MR Acquisition

Prior to the PET/MR imaging session, 5mCi of FDG was infused intravenously. During the FDG uptake period, patients were kept in a quiet room. 40 min after FDG infusion, patients were asked to empty their bladder prior to the imaging session. All images were acquired using a hybrid PET/MR scanner (Biograph mMR, Siemens HealthCare) housed in the Biomedical Research Imaging Center. A spine coil together with 2 anterior body coils were used to cover liver through kidneys. After acquiring localization images, MR attenuation images were acquired first, followed by a breath-hold T2 half-Fourier acquisition single-shot turbo spin-echo (HASTE) sequence. These included multiplanar T2 weighted images obtained sequentially 5mm in thickness with a 2 mm gap and pre and post contrast enhanced T1 weighted images obtained as a volume and reviewed as 3mm contiguous images in multiple planes. The dose of Gadolinium chelate (Gadopentetate dimeglumine) was 0.1 mg/kg over 1 minute using a standard delay protocol. A power injector was used to deliver contrast at 2cc/sec. This sequence was repeated twice along the coronal (cor) and axial orientations, respectively. The image parameters for the coronal orientation were as follows: repetition time, 2sec; echo time (TE) 94msec; slice thickness, 8 mm for 28 slices with 20% gap; matrix size, 256×256; acceleration factor of 3 using GRAPPA; flip angle, 150-degree; and voxel size 2×1.6×8mm3. In contrast, with the exception of TE=95msec, number of slices = 24, acceleration factor = 2, and voxel size = 1.7×1.4×8mm3, images acquired during a breath hold using an axial orientation used identical parameters as that for coronal orientation. The HASTE images were used for the placement of ROIs throughout the tumors. In contrast to MR imaging, a 4 min single-bed PET acquisition covering the kidneys was acquired simultaneously with the above outlined HASTE sequence. PET images were obtained on the same table again using a breath hold to reduce motion interference. Post procedure fusion of the MR and PET images with co-registration was performed using a dedicated workstation (Siemens Medical Solutions, Malvern, PA).

Image review

Two physicians reviewed images, one a genitourinary imaging specialist with 20 years experience and the other a nuclear medicine specialist with 15 years of experience. Cases were reviewed using a standardized hanging protocol. The high-resolution MR images were used to identify anatomic structures. Location of FDG and Gd uptake were identified,

focusing on the kidney tumor and local metastases. FDG uptake was quantified using standard uptake value (SUV). An increase of 2 SUV was considered increased avidity.

Antibodies and Immunohistochemistry

Rabbit polyclonal antibodies against CD31 (ab28364), FBP1 (HPA005857) and Glut-1(07-1401) were from Abcam (Cambridge, MA), Sigma Aldrich Corp. (St. Louis, MO) and Millipore (Billerica, MA)) respectively. Mouse monoclonal HIF-1α clone 54 (610959) was from BD Biosciences (San Jose, CA).

IHC was carried in the Bond Autostainer (Leica Biosystems Inc. Norwell, MA). Slides were dewaxed in Bond Dewax solution (AR9222) and hydrated in Bond Wash solution (AR9590). Antigen retrieval for all antibodies was performed for 30 min at 100ºC in Bond-Epitope Retrieval solution1 pH-6.0 (AR9961). After pretreatment slides were incubated with FBP1 (1:1500) and Glut-1 (1:2000) for 30 min, CD31 (1:200) for 1h and HIF-1α (1:100) for 3h. Detection of CD31, FBP1 and Glut-1 was performed using Bond™ Polymer Refine Detection (DS9900) and Bond™ Polymer Refine Red Detection (DS9390) for HIF-1α. Stained slides were dehydrated and coverslipped. Positive and negative controls (no primary antibody) were included for each antibody.

Digital imaging and image analysis

IHC stained slides were digitally imaged in the Aperio ScanScope XT (Leica) using 20x objective. HIF-1α, Glut-1 and FBP1 slides were analyzed using Aperio Image analysis algorithms and Definiens Tissue Studio software (Munich, Germany) was used to measure the microvessel density in CD31 stained slides.

Quantitative Image Analysis

For each subject, one PET image and five MRI images were analyzed as follows. The PET image was scaled to units of Standard Uptake Value (SUV). The MR images used included a T2-weighted HASTE sequence (referred to as “HASTE"), a water-content image from the Dixon sequence used for attenuation correction (referred to as “Water”), an apparent diffusion coefficient image (referred to as “ADC”), a t1-weighted image (referred to as “T1”), and a contrast image produced from the subtraction of pre-contrast from a post-contrast image (Referred to as “Contrast”). The ADC image was already quantified as an estimate of a physical quantity, the apparent diffusion coefficient, and was used unchanged. The other MRI images in their raw forms were quantified in arbitrary intensity units and so were normalized to the average intensity in a cortical region of the opposite healthy kidney.

Because the PET-MR scanner gives images that are already aligned, the PET and MRI images generally did not require an additional alignment step. However, in two cases, some images had to be rigidly translated to align the tumor sites; generally this appeared to be due to respiratory motion. All images were then resampled to the grid of the PET image (2.086 mm × 2.086 mm × 2.031 mm). Regions of interest encompassing the tumors were drawn by hand to isolate the tumor volume.

For each voxel, a set of six image quantities (PET, HASTE, Water, ADC, T1, and Contrast) were derived. Means of these six quantities within the tumor volume were computed for each subject. Further analysis of the PET image included computation of the percent of tumor volume exceeding certain SUV thresholds, which were found to be related to pathology outcomes.

Microarray Analysis

mRNA was extracted from fresh frozen ccRCC tissue specimens using the Qiagen AllPrep DNA/RNA Mini Kit (Valencia, CA), amplified, labeled and hybridized against a reference(9) on Agilent Whole Human Genome (4 × 44k) Oligo Microarrays. Missing data was imputed, log transformed (base 2), and median centered.

Subtype Classification

Samples were classified as either ccA or ccB using a reference microarray data set and centroid-based classification algorithm previously described(10).

The Cancer Genome Atlas (TCGA) data analysis

TCGA RNA sequence data were obtained from dbGAP and normalized to the upper quartile of normal counts. For analysis, the data were log-transformed (base 2) and genes were median centered.

Statistical Analysis

All statistical analyses were performed using the R program (R Project for Statistical Computing, Vienna, Austria). A two-sample Welch t-test was used to assess differences between subtypes, with all p-values lower than 0.05 considered significant. Gene and protein (H-Scores log2 transformed) expression data were fit with a mixed effects regression model using fixed effects for each variable of interest, and a random effect for the patients (nlme and lme4 R Packages). Standard errors of the effect estimates were calculated and illustrated as a forest plot. Intra-class correlation (ICC) was utilized to measure concordance between samples from the same patient and between patients. ICC was calculated for each pair and then summarized by mean for each group of paired samples. ICC values for unpaired groups were estimated from all samples in the group. Further analysis and plotting of paired and unpaired analyses were performed identically. The “irr” R package was used to generate ICC estimates.

Results

PET/MR imaging identifies heterogeneous regions in ccRCC

Medical imaging technologies, such as PET and MRI, have advanced the field of oncology by characterizing tumor morphology and disease monitoring. The fused PET/MR technology has further improved the assessment of soft-tissue for diagnostic purposes(11, 12). Functional imaging using PET has previously been evaluated in ccRCC to predict and evaluate response to systemic treatment(13, 14), but such studies have been challenged by the variable uptake of glucose in these tumors. Not surprisingly, this methodology has yet to

be adopted into general practice for screening or disease assessment(15, 16). In this study, we used PET/MR imaging to identify and evaluate heterogeneous regions of ccRCC (**Figure 1a and Supplemental Table 1**). MRI was used for its greater tissue resolution, and PET, as measured by standard uptake value (SUV), for mapping regional glucose uptake variation throughout the tumor. Various histologic morphologies were observed within these heterogeneous regions (**Supplemental Figure 1**), which ranged from the hallmark lipid-filled epithelial cells to granular cells with regional necrosis (**Figure 1b and Supplemental Table 2**), although notably, regional variation in SUV did not strictly correspond to regional necrosis.

We first evaluated levels of key proteins implicated in ccRCC in sampled tumor regions. Hypoxia inducible factors (HIF-1α and HIF-2α), are commonly stabilized in ccRCC due to the high frequency of *VHL* mutation in this disease(17, 18) and promote the expression of genes that support tumor progression, such as angiogenic factors like the vascular endothelial growth factor (VEGF) and the platelet endothelial cell adhesion molecule (PECAM)(19-21). Metabolic reprogramming is also central in tumor progression, especially in ccRCC(5, 22), with both glucose transporters (GLUT1) and key metabolic enzymes regulated by HIF factors. We detected regional variation in these features, and in particular we observed evidence of reduced protein (**Figure 1c and d**) and mRNA (**Figure 1e**) levels of the critical glycolytic enzyme FBP1. Specifically considering these factors directly regulate glucose metabolism, it was noteworthy to find that samples from PET avid regions expressed higher levels of glucose transporter GLUT1 and lower expression of FBP1 and the HIF-1α transcription factor (**Figures 1c-e**), potentially indicating a switch from storing energy to obtaining additional glucose to support increased metabolic activity(6). The acquisition of additional glucose may also be supported through an increased endothelial compartment that contains larger vessels, evident of the positive association between increased SUV and PECAM expression (Figure 1c and d). Downregulation of FBP1 was recently found to be a critical feature of progressive ccRCC(6) by enabling glycolytic flux in renal tubular epithelial cells, and this data further supports this mechanism.

ccRCC prognostic subtypes express heterogeneous biology

In addition to key ccRCC biological features, gene expression profiles which define low and high-risk patterns of ccRCC, clear cell A (ccA) and B (ccB) (10, 23-25) respectively, have also been observed to display regional heterogeneity(2, 25), possibly reflecting the same clonal evolution revealed in DNA sequencing studies. In our selected tumor samples, and similar to previous findings(2), intra-tumor gene expression heterogeneity was sometimes evident among samples from the same patient, although most tumors demonstrated a majority feature profile (**Figure 2a**) and similar expression profiles among intra-tumor samples (**Supplemental Figure S2**). In an effort to minimize the uncertainty surrounding the influence of tumor heterogeneity on gene expression(26, 27), we examined the relationship of the ccA/ccB subtyping with PET/MR imaging parameters, identifying PET standardized uptake value (SUV) to be the best for dichotomizing ccA patients from ccB (**Supplemental Figure S3**), even compared with a variety of MRI density measurements. Moreover, individually ccB-typed samples had significantly higher maximum SUV than ccA (Figure 2b). This maximum SUV also correlated with HIF-1α and GLUT1 protein levels,

which could account for the shift toward glucose uptake. No significant correlation was observed between subtype and HIF-2α (**Supplemental Figure S4**). FBP1 protein levels were significantly higher in good risk ccA classified samples and tumors (**Figure 2b**), suggesting a connection between possible alternate metabolic pathways and these ccRCC subtypes.

Metabolic activity dichotomizes ccRCC subtypes

Metabolic dysregulation has widely been considered as a fundamental event in ccRCC tumorigenesis due to the high frequency of *VHL* inactivation and resulting activation of HIF factors(28, 29), which regulate numerous genes involved in metabolism. Therapeutics are being developed and used to target enhanced metabolic pathways, such as the mTOR pathway. However, these agents produce either inefficient or varied patient responses, urging the need for a greater understanding of the complex relationships between tumor and host metabolic activities(30-33). Recently, the ccRCC cancer genome atlas (TCGA) elucidated that patients with unfavorable survival outcomes had higher expression of genes involved in early steps of glucose utilization, the oxidative pentose phosphate pathway, fatty acid synthesis, and downregulation of the PI(3)K pathway, whereas patients with better survival expressed genes involved in glycolysis, Krebs Cycle, and AMPK signaling(5). In our analysis, the ccA and ccB subtypes, and PET glucose uptake patterns, followed similar trends, as ccB (SUV high) samples significantly displayed higher expression levels of oxidative pentose phosphate pathway genes whereas ccA (SUV low) samples had higher levels of glycolytic and Krebs Cycle genes (**Figure 3a**).

Surprisingly, FBP1 and other glucose storage genes showed differential expression between ccA and ccB-typed samples. It was recently demonstrated that FBP1 is frequently depleted in ccRCC and may act as a critical mediator of tumor progression(6). We observed that the majority of ccB-typed samples have depleted FBP1 transcript levels, as compared to ccA, consistent with FBP1 loss corresponding to steps in disease progression or an aggressive phenotype. Similarly, a metabolic switch was evident between ccA and ccB assigned samples in the TCGA dataset. ccA samples demonstrated notably higher glycogen synthesis (**Figure 3b**), glycolysis (**Figure 3c**), and Krebs Cycle (**Figure 3d**) activity compared to ccB samples that had enhanced oxidative pentose phosphate (**Figure 3e**) and mTOR pathway (**Figure 3f**) activation. The trend towards a “Warburg effect”-like state identified in the ccRCC TCGA was evident with ccA patients who experienced increased AMPK signaling (**Figure 3g**) and expression of mTOR pathway inhibition, as compared to the upregulation of fatty acid synthesis in ccB patients (**Figure 3h**).

Distinct metabolic pathways predict subtypes

We performed logistic regression on both ccA and ccB samples from our study samples (**Figure 4a**) and those from the TCGA (**Figure 4b**) to identify biological variables significantly correlated to and predictive of subtype. In our study, ccA samples were best defined by genes (pink) and proteins (purple) involved in glucose storage and glycolysis (**Figure 4a**). On the other hand, enhanced expression of pentose phosphate pathway genes distinguished ccB samples. Higher standard uptake values trended towards ccB (p-value=0.06), however the sample size prevented statistical significance. We were able to

further evaluate metabolic trends that characterized the two subtypes by using RNA-seq data from the TCGA (**Figure 4b**). Similar to previous findings, the most significant genes associated with the ccA subtype involved the upregulation of glycogen synthesis (G6PC, FBP1, PCK1, and PCK2), glycolysis (PKLR, ENO1, LDHD, LDHA, and PGK1), and Krebs Cycle (PDK2, PDK1, ACO2, SDHC, SDHB) in contrast to ccB samples which had significant association with the oxidative pentose phosphate pathway (HK3, PGLS, G6PC, TKT, PGD, and PFKM) and fatty acid synthesis (FASN, ACACA, and ME1). Interestingly, the PI(3)K pathway inhibitors TSC1 and GRB10 were highly associative to the ccA subtype, while mTOR genes (mTOR and RHEB) were enhanced in ccB subtype, again, highlighting metabolic redirection in these two prognostic groups (**Figure 5**).

FDG uptake correlates to tumor heterogeneity

Intra-tumor heterogeneity has been shown to significantly impact the genome of ccRCC creating difficulties in revealing underlying molecular events that promote tumorigenesis and progression(1, 2). Thus, biomarkers are urgently needed that provide insight towards tumor biological processes, and which have the potential to comprehensively assess the whole disease(32, 34, 35). We observed a wide range of contrast patterns in our ccRCC patients, including patterns displaying low or no FDG uptake (**Figure 6a**), and tumors that displayed uniformly high SUV (**Figure 6b**). Furthermore, patients who expressed a complete or predominately ccB subtype had SUVs of 2.0 or higher in 50% or more of the tumor volume compared to only 20% or less in tumors of ccA patients (**Figure 6c**). Thus, utilizing PET/MR can potentially facilitate personalized tumor evaluations without using invasive alternatives, especially where biopsy bias is a concern(27).

Discussion

In this study, we provide further evaluation of the effector products of tumor heterogeneity, finding variation in metabolic and angiogenic gene, protein, and tissue features. In addition, we present a novel approach incorporating functional imaging with multiregional gene expression profiling to facilitate the assessment of intra-tumor heterogeneity and tumor progression. This technique can potentially facilitate a comprehensive assessment of the tumor without using invasive alternatives, especially where biopsy bias is a concern(27).

The ccRCC subtypes, ccA and ccB, even as defined based on single tissue sample specimens, have been validated as prognostic tools for this disease. ccA patients have substantially better cancer-specific and recurrence-free survival than patients of the ccB subtype (10). However, intratumor heterogeneity has been observed for this gene expression feature set; therefore, a secondary tool that can provide a holistic evaluation of the patient's disease would be highly valuable in selecting regions for sampling. Here, we have identified that ccB samples express higher glucose uptake compared to ccA and tumors with any ccB-typed regions have higher overall SUV tumor means compared to ccA. Thus, PET imaging could be used in the future to guide biopsy or sample collection for biomarker analysis, or the patterns of SUV present in tumors could be further studied as an independent non-invasive biomarker for classifying tumor risk.

This study also underscores the potential importance of metabolic transitions in the progression of ccRCC, with FBP1 expression as a potentially key factor. ccA tumor cells appear to produce energy through increased glycolysis and Krebs Cycle activity, while storing additional glucose (and thus, potentially not requiring high levels of uptake) through FBP1-controlled glycogen synthesis, in keeping with the glycogen-rich histology that is classic for lower grade ccRCC tumors. In contrast, metabolic activity in ccB patients is substantially enhanced, with glucose uptake and synthesis increased and storage decreased. The oxidative pentose phosphate pathway is elevated and potentially functions as a generator of NADPH for ccB patients, which is likely supported via the mTOR pathway (**Figure 5**). This finding is in keeping with the original observation that mTOR pathway activation occurred later in disease progression, eventually leading to the indication for mTOR inhibitor temsirolimus being applied for poor risk patients(36).

This preliminary study is limited by the relatively smaller available sample size, but recapitulates the approximate levels of heterogeneity observed in the genotype driven studies of similar scale(1, 2). In addition, the relatively low SUV of ccRCC tumors overall both provided us with a good window for discrimination (in contrast to tumor types that are consistently strikingly high for SUV), and utilizes values that have conventionally bordered on the level of detection when compared with CT/PET. PET/MR is an emerging technology that provides enhanced tissue and spatial resolution for discrete sampling of regions of interest, and newer evidence suggests that reported SUVs are typically lower with PET/MR(37), and re-evaluation of thresholds is likely to be considered as this technology matures. PET/MR provided the opportunity to explore a variety of dynamic contrast enhancement features, none of which provided a clear association with the tissue biological features we investigated in exploring the heterogeneity of ccRCC. However, the high level of architectural resolution was very useful for tracking the regions of interest across imaging and tissue collection. Future studies examining regional PET as an independent prognostic factor should consider the technological differences of CT/PET compared with PET/MR.

Another particularly interesting future question would be to examine how this applies in assessing metastatic disease, where differential metabolic activity may be informative for predicting response to therapy. A previous study examined CT/PET as a biomarker of response to everolimus, but was challenged by the heterogeneity of signal in metastatic disease(38). However, as we have shown here, this may be reflective of differing underlying biology.

Future studies are required to validate the metabolic mechanisms of the ccA and ccB subtypes. However, this is the first study to evaluate the correspondence of regional variations in tissue features with imaging parameters that can be assessed over defined regions of interest. These findings suggest novel properties of regional tumor variation that may improve assessment for prognostic and predictive outcomes for ccRCC, and shed light on metabolic transitions that accompany the switch to more aggressive disease.

Supplementary Material

Refer to Web version on PubMed Central for supplementary material.

Acknowledgements

This work was supported by a grant from the UNC Biological Research Imaging Center and NIH award K24CA172355 to W.K. Rathmell; National Research Service Award T32ES007126 from the National Institute of Environmental Health Sciences to S. Brooks; the Howard Hughes Medical Cancer Institute of the National Institutes of Health Award 5T32CA160001. We thank Nana N. Feinberg and Bentley R. Midkiff in the UNC Translational Pathology Laboratory (TPL) for expert technical assistance. The UNC Translational Pathology Laboratory is supported in part, by grants from the National Cancer Institute (3P30CA016086) and the UNC University Cancer Research Fund (UCRF). Dr. Nielsen's contribution is supported in part by the American Cancer Society (Grant MRSG-13-154-01-CPPB) and the Urology Care Foundation / Astellas (Rising Stars in Urology Research Award).

References

1. Gerlinger M, Horswell S, Larkin J, Rowan AJ, Salm MP, Varela I, et al. Genomic architecture and evolution of clear cell renal cell carcinomas defined by multiregion sequencing. Nat Genet. 2014; 46:225–33. [PubMed: 24487277]
2. Gerlinger M, Rowan AJ, Horswell S, Larkin J, Endesfelder D, Gronroos E, et al. Intratumor heterogeneity and branched evolution revealed by multiregion sequencing. N Engl J Med. 2012; 366:883–92. [PubMed: 22397650]
3. Sankin A, Hakimi AA, Mikkilineni N, Ostrovnaya I, Silk MT, Liang Y, et al. The impact of genetic heterogeneity on biomarker development in kidney cancer assessed by multiregional sampling. Cancer Med. 2014; 3:1485–92. [PubMed: 25124064]
4. Gordan JD, Lal P, Dondeti VR, Letrero R, Parekh KN, Oquendo CE, et al. HIF-alpha effects on c-Myc distinguish two subtypes of sporadic VHL-deficient clear cell renal carcinoma. Cancer Cell. 2008; 14:435–46. [PubMed: 19061835]
5. Network TCGR. Comprehensive molecular characterization of clear cell renal cell carcinoma. Nature. 2013; 499:43–9. [PubMed: 23792563]
6. Li B, Qiu B, Lee DS, Walton ZE, Ochocki JD, Mathew LK, et al. Fructose-1,6-bisphosphatase opposes renal carcinoma progression. Nature. 2014; 513:251–5. [PubMed: 25043030]
7. Network TCGR. The somatic genomic landscape of chromophobe renal cell carcinoma. Cancer Cell. 2014; 26:319–30. [PubMed: 25155756]
8. Network TCGAR. Comprehensive Molecular Characterization of Papillary Renal Cell Carcinoma. New England Journal of Medicine. 2015 Manuscript submitted.
9. Perou CM, Sorlie T, Eisen MB, van de Rijn M, Jeffrey SS, Rees CA, et al. Molecular portraits of human breast tumours. Nature. 2000; 406:747–52. [PubMed: 10963602]
10. Brooks SA, Brannon AR, Parker JS, Fisher JC, Sen O, Kattan MW, et al. ClearCode34: A prognostic risk predictor for localized clear cell renal cell carcinoma. European Urology. 2014; 66:77–84. [PubMed: 24613583]
11. Catana C, Drzezga A, Heiss WD, Rosen BR. PET/MRI for neurologic applications. J Nucl Med. 2012; 53:1916–25. [PubMed: 23143086]
12. Drzezga A, Souvatzoglou M, Eiber M, Beer AJ, Furst S, Martinez-Moller A, et al. First clinical experience with integrated whole-body PET/MR: comparison to PET/CT in patients with oncologic diagnoses. J Nucl Med. 2012; 53:845–55. [PubMed: 22534830]
13. Braunagel M, Graser A, Reiser M, Notohamiprodjo M. The role of functional imaging in the era of targeted therapy of renal cell carcinoma. World Journal of Urology. 2014; 32:47–58. [PubMed: 23588813]
14. Khandani AH, Cowey CL, Moore DT, Gohil H, Rathmell WK. Primary renal cell carcinoma: relationship between 18F-FDG uptake and response to neoadjuvant sorafenib. Nucl Med Commun. 2012; 33:967–73. [PubMed: 22714005]
15. Miyakita H, Tokunaga M, Onda H, Usui Y, Kinoshita H, Kawamura N, Yasuda S. Significance of 18F-fluorodeoxyglucose positron emission tomography (FDG-PET) for detection of renal cell carcinoma. International Journal of Urology. 2002; 9:15–8. [PubMed: 11972644]
16. Namura K, Minamimoto R, Yao M, Makiyama K, Murakami T, Sano F, et al. Impact of maximum standardized uptake value (SUVmax) evaluated by 18-Fluoro-2-deoxy-D-glucose positron

emission tomography/computed tomography (18F-FDG-PET/CT) on survival for patients with advanced renal cell carcinoma: a preliminary report. BMC Cancer. 2010; 10:667. [PubMed: 21129184]

17. Latif F, Tory K, Gnarra J, Yao M, Duh FM, Orcutt ML, et al. Identification of the von Hippel-Lindau disease tumor suppressor gene. Science. 1993; 260:1317–20. [PubMed: 8493574]
18. Brooks SA, Rathmell WK. Uniting Molecular Biomarkers to Advance the Science and Care of Clear Cell Renal Cell Carcinoma. The Journal of OncoPathology. 2014; 1:45–54.
19. Pennacchietti S, Michieli P, Galluzzo M, Mazzone M, Giordano S, Comoglio PM. Hypoxia promotes invasive growth by transcriptional activation of the met protooncogene. Cancer Cell. 2003; 3:347–61. [PubMed: 12726861]
20. Petrella BL, Lohi J, Brinckerhoff CE. Identification of membrane type-1 matrix metalloproteinase as a target of hypoxia-inducible factor-2 alpha in von Hippel-Lindau renal cell carcinoma. Oncogene. 2005; 24:1043–52. [PubMed: 15592504]
21. Smith K, Gunaratnam L, Morley M, Franovic A, Mekhail K, Lee S. Silencing of epidermal growth factor receptor suppresses hypoxia-inducible factor-2-driven VHL-/- renal cancer. Cancer Res. 2005; 65:5221–30. [PubMed: 15958567]
22. Linehan WM, Rathmell WK. Kidney cancer. Urol Oncol. 2012; 30:948–51. [PubMed: 23218074]
23. Brannon AR, Haake SM, Hacker KE, Pruthi RS, Wallen EM, Nielsen ME, et al. Meta-analysis of Clear Cell Renal Cell Carcinoma Gene Expression Defines a Variant Subgroup and Identifies Gender Influences on Tumor Biology. European Urology. 2012; 61:258–68. [PubMed: 22030119]
24. Brannon AR, Reddy A, Seiler M, Arreola A, Moore DT, Pruthi RS, et al. Molecular Stratification of Clear Cell Renal Cell Carcinoma by Consensus Clustering Reveals Distinct Subtypes and Survival Patterns. Genes & Cancer. 2010; 1:152–63. [PubMed: 20871783]
25. Gulati S, Martinez P, Joshi T, Birkbak NJ, Santos CR, Rowan AJ, et al. Systematic evaluation of the prognostic impact and intratumour heterogeneity of clear cell renal cell carcinoma biomarkers. European Urology. 2014; 66:936–48. [PubMed: 25047176]
26. Tomaszewski JJ, Uzzo RG, Smaldone MC. Heterogeneity and renal mass biopsy: a review of its role and reliability. Cancer Biol Med. 2014; 11:162–72. [PubMed: 25364577]
27. Volpe A, Finelli A, Gill IS, Jewett MA, Martignoni G, Polascik TJ, et al. Rationale for percutaneous biopsy and histologic characterisation of renal tumours. European Urology. 2012; 62:491–504. [PubMed: 22633318]
28. Clifford SC, Prowse Amanda H. Affara Nabeel A. Buys Charles H.C.M. Maher Eamonn R. Inactivation of the von Hippel–Lindau (VHL) Tumour Suppressor Gene and Allelic Losses at Chromosome Arm 3p. GENES, CHROMOSOMES & CANCER. 1998; 22:200–9. [PubMed: 9624531]
29. Nickerson ML, Jaeger E, Shi Y, Durocher JA, Mahurkar S, Zaridze D, et al. Improved identification of von Hippel-Lindau gene alterations in clear cell renal tumors. Clin Cancer Res. 2008; 14:4726–34. [PubMed: 18676741]
30. Sternberg CN, Davis ID, Mardiak J, Szczylik C, Lee E, Wagstaff J, et al. Pazopanib in locally advanced or metastatic renal cell carcinoma: results of a randomized phase III trial. J Clin Oncol. 2010; 28:1061–8. [PubMed: 20100962]
31. Motzer RJ, Hutson TE, Tomczak P, Michaelson MD, Bukowski RM, Rixe O, et al. Sunitinib versus interferon alfa in metastatic renal-cell carcinoma. N Engl J Med. 2007; 356:115–24. [PubMed: 17215529]
32. Vasudev NS, Selby PJ, Banks RE. Renal cancer biomarkers: the promise of personalized care. BMC Med. 2012; 10:112. [PubMed: 23016578]
33. Motzer RJ, Bukowski RM. Targeted therapy for metastatic renal cell carcinoma. J Clin Oncol. 2006; 24:5601–8. [PubMed: 17158546]
34. Sanjmyatav J, Steiner T, Wunderlich H, Diegmann J, Gajda M, Junker K. A specific gene expression signature characterizes metastatic potential in clear cell renal cell carcinoma. J Urol. 2011; 186:289–94. [PubMed: 21600596]
35. Smaldone MC, Fung C, Uzzo RG, Haas NB. Adjuvant and neoadjuvant therapies in high-risk renal cell carcinoma. Hematol Oncol Clin North Am. 2011; 25:765–91. [PubMed: 21763967]

36. Hudes G, Carducci M, Tomczak P, Dutcher J, Figlin R, Kapoor A, et al. Temsirolimus, interferon alfa, or both for advanced renal-cell carcinoma. N Engl J Med. 2007; 356:2271–81. [PubMed: 17538086]

37. Wiesmuller M, Quick HH, Navalpakkam B, Lell MM, Uder M, Ritt P, et al. Comparison of lesion detection and quantitation of tracer uptake between PET from a simultaneously acquiring whole-body PET/MR hybrid scanner and PET from PET/CT. Eur J Nucl Med Mol Imaging. 2013; 40:12–21. [PubMed: 23053323]

38. Chen JL, Appelbaum DE, Kocherginsky M, Cowey CL, Rathmell WK, McDermott DF, et al. FDG-PET as a predictive biomarker for therapy with everolimus in metastatic renal cell cancer. Cancer Med. 2013; 2:545–52. [PubMed: 24156027]

Translational Relevance

The incidence of adult Renal Cell Carcinoma, or kidney cancer, is on a steady rise in the western world. There are multiple subtypes of this disease, the most frequent type, clear cell Renal Cell Carcinoma (ccRCC), is closely linked to hypoxia signaling through the high frequency loss of the VHL gene. ccRCC has recently been redefined as a highly heterogeneous disease. Here, we used positron emission tomography with magnetic resonance (PET/MR) imaging to better understand how tumor heterogeneity affects tumor biology through variations in hypoxia signaling, metabolism, vascularity, and gene expression signatures to provide fortitude towards individual patient treatment options. Utilizing these tools prior to surgical resection has the potential to reveal links between biological correlates and imaging parameters that can prevent unnecessary invasive procedures and enable enhanced knowledge of the relationships of heterogeneity and ccRCC.

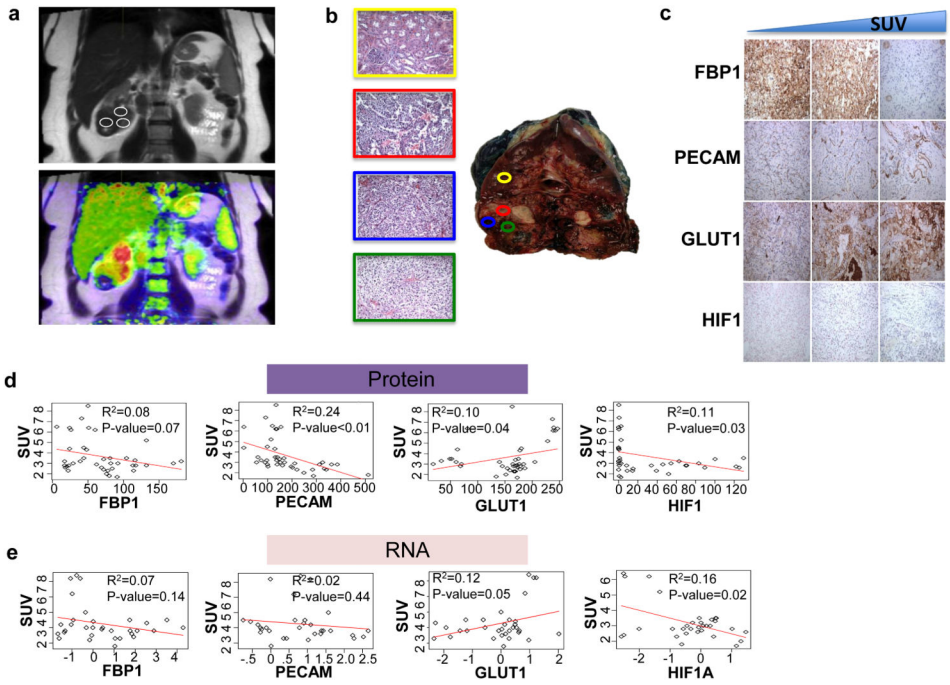

Figure 1. PET/MR imaging characterizes heterogeneous regions of ccRCC that correlate to tumor biology

(**a**) Tumor samples were obtained from eight ccRCC patients for hematoxylin and eosin (**b**), immunohistochemistry (**c** and **d**), and microarray (**e**) analysis. (**b**) Normal kidney cortex architecture was observed in the normal tissue (yellow) compared to ccRCC (red, blue, and green) that displayed various architectures that ranged from classical epithelial cells with clear cytoplasm and distinct membranes to a granular cell morphology. Samples with increased Glut1 protein (**c** and **d**) and gene expression (**e**) correlated with higher Fluorodeoxyglucose uptake (SUV), suggesting a possible mechanism that supports the greater metabolic activity. In contrast, protein (**c** and **d**) and gene expression (**e**) of the fructose-1,6-bisphosphatase 1 (FBP1) enzyme and the hypoxia inducible factor 1 (HIF-1α) were anti-correlative to SUV. The expression density of the platelet endothelial cell adhesion molecule (PECAM) decreased with higher SUV, but revealed larger vessels with high PET avidity.

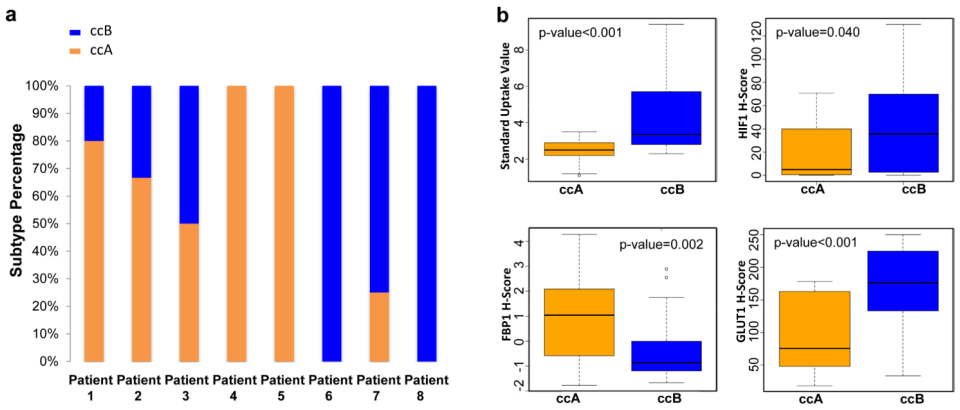

Figure 2. PET dichotomizes ccRCC subtypes by metabolic activity

Heterogeneous subtype classification was evident among samples from the same patient (**a**). However, an overall classification trend was observed with all patients. All primary tumor samples from Patient 3 were of the ccA subtype and metastatic samples ccB. (**b**) ccB samples had significantly higher maximum SUV compared to ccA, as well as increased expression of HIF-1α and activation of the glucose transporter GLUT1. Interestingly, ccA and ccB-typed samples expressed distinct levels of FBP1, suggesting discrete metabolic reprogramming within these two groups.

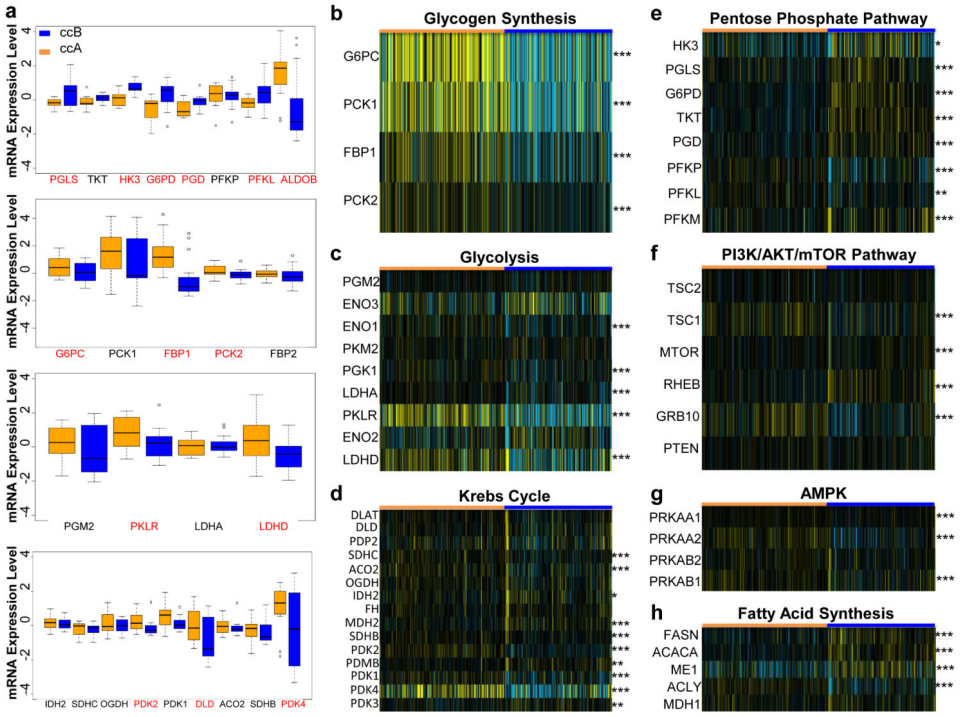

Figure 3. ccRCC subtypes are involved in distinct metabolic pathways

Increased metabolic activity is a key event in ccRCC progression and has been postulated to be a future target for personalized treatment. (**a**) ccB patients had significantly higher expression of genes associated with the oxidative pentose phosphate pathway (PGLS, HK3, G6PD, PGD, PFKL, and ALDOB), while having lower levels of genes involved in glucose storage (G6PC, FBP1, and PCK2), showing a shift in metabolism towards glucose synthesis. On the other hand, glycolytic activity (PKLR and LDHD) was enhanced in ccA samples compared to ccB, as well as Kreb Cycle genes (PDK2, DLD, and PDK4). Red genes were found statistically significant (p-value>0.05) between ccA and ccB samples by a Welsh t-test. Similar to the patients in the study, ccA and ccB patients from the ccRCC Cancer Genome Atlas (TCGA) (**b-h**) separated by the activation of distinctive metabolic pathways. ccA patients had higher expression of genes associated with glucose storage (**b**), glycolysis (**c**), and the Krebs Cycle (**d**) compared to ccB patients. Much like ccB patients in **Figure 3a**, ccB patients had higher expression of genes involved in the oxidative phase of the pentose phosphate pathway (**e**). Interestingly, ccA patients significantly increased expression of genes inhibiting the PI(3)K, AKT, and MTOR pathway (**f** and **g**), while ccB patients had activation of the mTOR pathway and fatty acid synthesis (**h**), suggesting a possible mechanism for increased HIF-1α and GLUT1 expression in ccB patients (**Figure 2d**). Welsh t-test was performed to analyze significance of gene expression between subtypes (* = p-value>0.05, ** = p-value>0.01, *** = p-value>0.001).

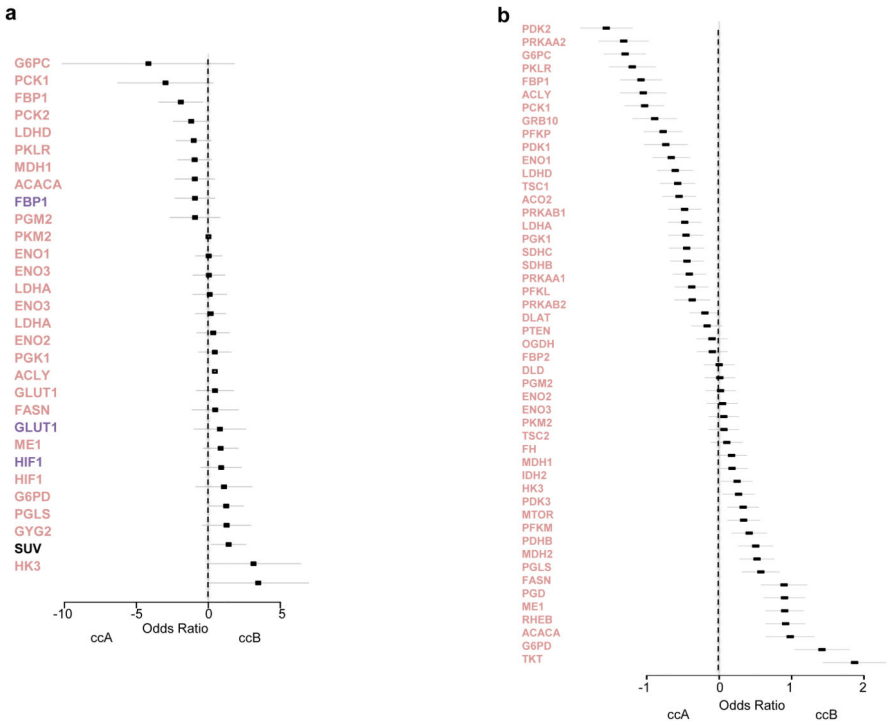

Figure 4. Distinct pathways support ccRCC metabolism

Logistic regression was performed to assess which biological features were significantly correlated to the ccA and ccB subtypes, with the exclusion of patient effect. (**a**) A forest plot depicts the association of effect estimates (odds ratios) of genes (pink), proteins (purple), and standard uptake values (black) with ccA (odds ratios between −10 and −1) and ccB subtypes (odds ratios between 1 and 5). The G6PC and PCK1 genes were highly associated with ccA samples, but weren't significantly valuable. However, FBP1 gene expression was significantly correlated and higher in (p-value=0.014) ccA samples. In contrast, ccB samples were associated with the gene expression of G6PD (p-value=0.042) and HK3 (p-value=0.052), as well as SUV (p-value=0.06). (**b**) Similar metabolic trends were associated with subtype in the ccRCC TCGA, where enhanced expression of glycogen synthesis (G6PC, FBP1, PCK1, and PCK2), glycolysis (PKLR, ENO1, LDHD, LDHA, and PGK1) and Krebs Cycle (PKLR, ENO1, LDHD, LDHA, and PGK1) genes were associated with ccA, while oxidative pentose phosphate pathway (HK3, PGLS, G6PC, TKT, PGD, and PFKM) and fatty acid synthesis (FASN, ACACA, and ME1) genes were upregulated in ccB.

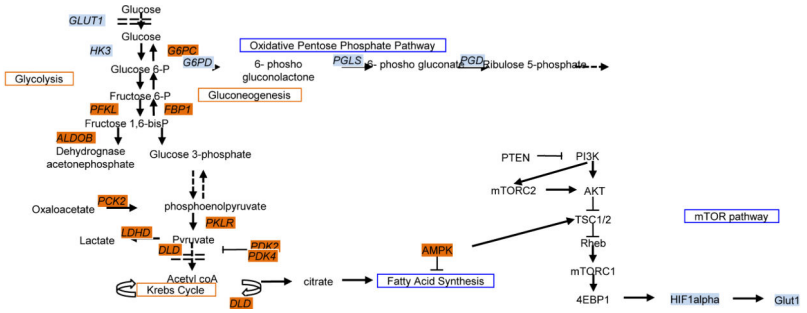

Figure 5. Metabolic pathways expressed in ccRCC subtypes

A model illustrating the different metabolic pathways driving the ccA (orange) and ccB (blue) subtypes. ccAs generate NADH for the electron transport pathway mainly through glycolysis and Krebs Cycle, while fatty acid synthesis is enhanced to generate energy through the oxidative pentose phosphate pathway in ccBs. The mTOR pathway activity is also enhanced in ccBs driving the expression of HIF-1α and thus the target gene GLUT1, resulting in higher glucose uptake.

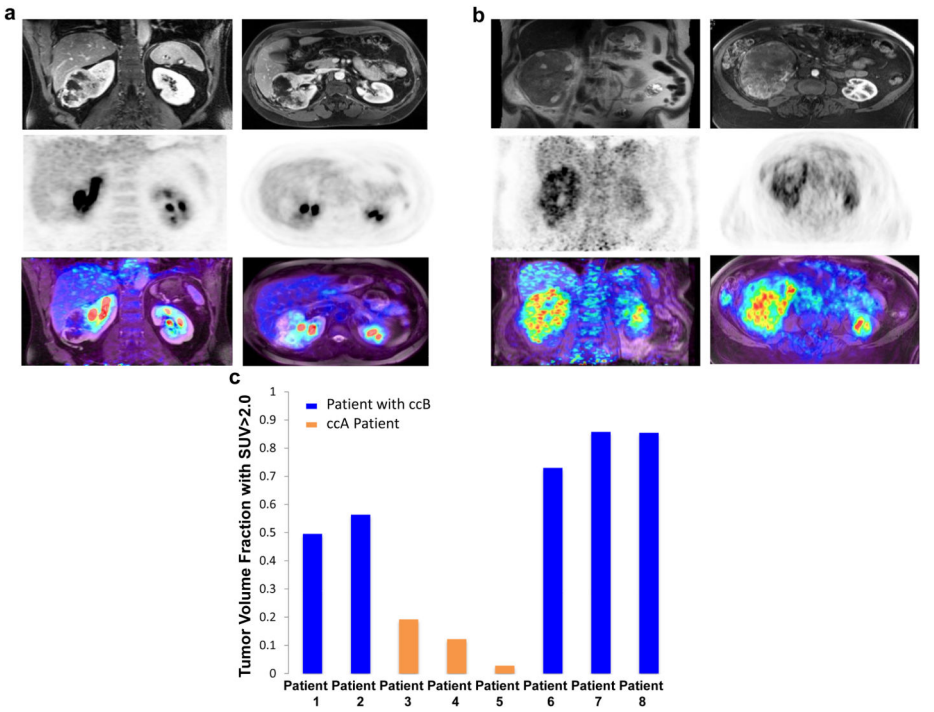

Figure 6. FDG uptake correlates to ccRCC heterogeneity

Representative PET, MR, and PET/MR fused images depicting low (**a**) and high (**b**) metabolic activity in clear cell Renal Cell Carcinoma (ccRCC). Patients who largely expressed the ccA classification profile were considered ccA and those expressing mostly ccB were considered ccB. Only the primary tumor was used to measure tumor means, so Patient 3 was annotated as a ccA patient (**c**). Standardized Uptake Value (SUV) of primary tumors was greater than 2.0 in at least 50% of tumor volume for tumors with a ccB classification while those absent of ccB exceeded SUV of 2.0 in 20% or less of tumor volume.